applied sciences

MDPI

Article

Assessment of Hot-Pressing Sintering Effect of Skutterudite $In_{0.40}Mn_{0.15}Co_{3.85}Sb_{12}$, Structure, Optical, and Electrical Properties

Silvana Moris [1], Nicolás Araya [2], Rodrigo Castillo [3], Paulina Valencia-Gálvez [4,*] and Catalina Cortés [5,*]

[1] Centro de Investigación de Estudios Avanzados del Maule (CIEAM), Vicerrectoría de Investigación y Postgrado, Universidad Católica del Maule, Avenida San Miguel 3605, Talca 3480112, Chile; smoris@ucm.cl
[2] Departamento de Ingeniería de Materiales, Facultad de Ingeniería, Universidad de Concepción, Concepción 4070386, Chile; nicolasiaraya@udec.cl
[3] Departamento de Química Inorgánica, Facultad de Química y de Farmacia, Pontificia Universidad Católica de Chile, Santiago 7820436, Chile; rodrigo.castillo@uc.cl
[4] Departamento de Química, Universidad Técnica Federico Santa María, Campus San Joaquín, Santiago 8940000, Chile
[5] Departamento de Química, Facultad de Ciencias, Universidad de Chile, Las Palmeras 3425, Santiago 780000, Chile
* Correspondence: paulina.valencia@usm.cl (P.V.-G.); cata89@uchile.cl (C.C.)

Abstract

In this study, $In_{0.40}Mn_{0.15}Co_{3.85}Sb_{12}$ was synthesized by the ceramic method, using a traditional melting–annealing treatment (MA), followed by grinding and sintering via the hot-pressing (HP) technique. Rietveld refinement of the powder diffraction (PXRD) data confirms that the resulting phase has a cubic crystal structure in space group *Im-3*, which is isostructural with the pristine Co_4Sb_{12} phase. The cell parameter *a* of the filled $In_{0.40}Mn_{0.15}Co_{3.85}Sb_{12}$ increases after hot pressing compared with the Co_4Sb_{12} phase. This suggests that the partial substitution of cobalt atoms with manganese (Mn) alters the cell size of the resulting material. The PXRD pattern of the $In_{0.40}Mn_{0.15}Co_{3.85}Sb_{12}$ phase of the MA sample shows a low-intensity line (~30°), which is related to elemental antimony (~4%, by Rietveld refinement). Rietveld refinements support a second model which implies the pressure-induced self-insertion of remanent antimony from the (MA) phase into the void sites after (HP) treatment, leading to a new phase: $In_{0.30}Sb_{0.10}Mn_{0.15}Co_{3.85}Sb_{11.90}$ (HP). The vibrational Raman modes of the obtained phases, $In_{0.40}Mn_{0.15}Co_{3.85}Sb_{12}$ (MA and HP), are correlated with those of the pristine phase, Co_4Sb_{12}. A strong primary signal at 185 cm^{-1} in the Raman spectrum of $In_{0.40}Mn_{0.15}Co_{3.85}Sb_{12}$ (MA) is associated with antimony impurities, which is confirmed by Rietveld refinement. Raman spectra of the HP sample are well correlated to the (SPS) Co_4Sb_{12} phase, which reveals structural changes due to self-insertion of antimony into the voids. The band-gap energy values of both the $In_{0.40}Mn_{0.15}Co_{3.85}Sb_{12}$ (MA) phase and the (HP) phase are 0.750 ± 0.006 eV and 0.650 ± 0.004 eV, respectively. These values are higher than those of the Co_4Sb_{12} phase, which has a band-gap energy of 0.55 eV. This indicates that the electronic band structure is modified by the partial substitution of cobalt with manganese and the introduction of indium in the icosahedral cages. Electrical transport properties at room temperature show that $In_{0.40}Mn_{0.15}Co_{3.85}Sb_{12}$ (MA) and $In_{0.30}Sb_{0.10}Mn_{0.15}Co_{3.85}Sb_{11.90}$ (HP) are n-type semiconductors.

Keywords: inorganic materials; electrical properties; skutterudites

Check for updates

Academic Editor: João Lourenço

Received: 13 April 2026
Revised: 16 May 2026
Accepted: 20 May 2026
Published: 24 May 2026

Copyright: © 2026 by the authors. Licensee MDPI, Basel, Switzerland. This article is an open access article distributed under the terms and conditions of the Creative Commons Attribution (CC BY) license.

1. Introduction

In the last few decades, there have been constant efforts to resolve the electric energy problem through clean environmental processes to reduce the emission of greenhouse gases. In prominent cases, those processes carry an inevitable heat loss to the environment. The waste heat can be used by implementing thermoelectric materials [1–4]. Thermoelectric devices are usually solid-state materials that directly convert thermal energy to electrical energy without intermediates. Thomas Seebeck discovered the effect of heat conversion on electric conductivity in 1821 [5]. This effect occurs using a thermoelectric device equipped with two legs of semiconductor material, *n*-type and *p*-type; the two legs are electrically connected in series and thermally connected in parallel. When a heat gradient is applied to one side of the legs, charge carriers in the thermoelectric device will move from the hot side to the cold side. Finally, charge-carrier movement produces a potential difference, ΔV, across the material. To evaluate the thermoelectric efficiency of the material, the dimensionless parameter ZT is evaluated [6]:

$$ZT = \frac{S^2\sigma}{\kappa_t} T \quad (1)$$

where S is the Seebeck coefficient, σ is the electrical conductivity, $\kappa_t = \kappa_e + \kappa_L$ is the total thermal conductivity, and T is the absolute temperature. Commercial efficiency should be at least ZT = 3 [7]. High S, high σ, and low values of κ_t are essential to good thermoelectric performance. However, S, σ, and κ_t cannot be optimized simultaneously. High values of S imply low conductivity values, and total thermal conductivity depends on lattice thermal conductivity and electronic contribution (Wiedemann–Franz law): $\kappa_e = L\sigma T$ [8]. Electrical conductivity ($\sigma = ne\mu$) depends on charge-carrier mobility (μ), the number of charge carriers (n), and the charge of the carrier (e). Materials with high thermoelectric performance are commonly heavily doped semiconductors with charge-carrier concentrations ranging from 10^{19} to 10^{21} cm^{-3} [9]. In these scenarios, finding a thermoelectric material with excellent performance has been challenging. Thermoelectric materials have been studied since the 20th century, especially heavily doped tellurium-based semiconductors such as Bi_2Te_3 [4]. These materials have been widely studied for low-temperature thermoelectric conversion, such as cooling in refrigerators or coolers [1]. However, at high temperatures (above 400K), their power generation declines. In contrast, skutterudites are a promising alternative for mid- to high-temperature thermoelectric applications (400–800 K), such as industrial waste heat conversion, where operating temperatures are naturally high.

In recent years, skutterudites have been extensively studied due to their excellent transport properties, such as high carrier mobility, which are valuable for thermoelectric applications [10,11].

Skutterudites have the general formula TPn_3, where T is a transition metal and Pn is a pnictogen (Pn = Sb, As, or P). Skutterudites have a cubic crystallographic structure with a space group *Im-3*. The unit cell comprises 32 atoms (eight octahedra formed by transition metal and pnictogen atoms) and two voids with icosahedral shapes, and some pnictogen atoms form rings of four pnictogen atoms each (Figure 1) [12].

Co_4Sb_{12} skutterudites have been widely studied because of their unique structure and physical properties. The icosahedral voids in Co_4Sb_{12} materials are about 1.892 Å in size [13], allowing them to host guest atoms or "fillers" that interact weakly with the Sb_4 rings inside the voids.

Electropositive elements such as alkali metals [14], alkaline earth metals [15], and lanthanides [16] have been widely used as filler atoms. These filler atoms can significantly alter the material's transport properties by acting as charge-carrier donors. [17].

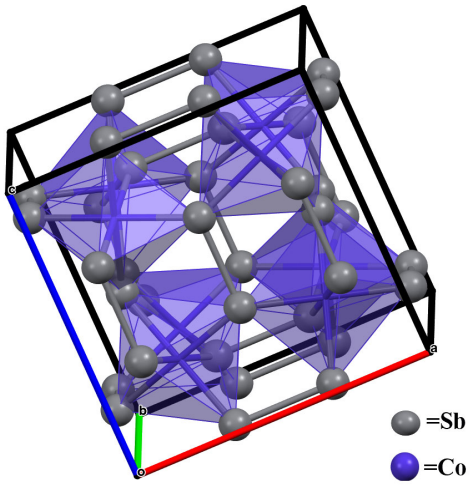


Figure 1. Crystal structure of Co_4Sb_{12} phase. The colored lines are the axes in 3Dspace. Red: axis a, green: axis b, blue: axis c.

It has been reported that the electrical transport properties of Co_4Sb_{12}-based skutterudites have been improved by inserting positively charged fillers into the icosahedral voids, as the fillers can donate extra charge carriers to the system, thereby enhancing electrical conductivity [9]. For example, substitution of indium atoms into the icosahedral voids in the Co_4Sb_{12} system has been widely studied, in which the filler substituent acts as an electron donor [18–20]. Khovaylo et al. reported that upon progressive substitution of indium into the voids of Co_4Sb_{12} skutterudite, the electrical conductivity increases and the thermal conductivity decreases, resulting in high thermoelectric performance [21].

On the other hand, studies have shown that transport properties of Co_4Sb_{12}-based materials can be modified by altering their chemical composition through the incorporation of dopant elements that replace cobalt with other transition metals, such as Fe [22], Ni [23], or Mn [24]. Dopants play the role of supplying charge carriers to the system to improve the transport properties of the material. For example, the partial substitution of cobalt atoms with manganese atoms in the pristine phase of Co_4Sb_{12} and Sn by Sb sites was explored by Park et al. They found that as the concentration of manganese dopants increases in the Co_4Sb_{12} system, the charge carriers (holes) increase by two orders of magnitude; nevertheless, when the Sn dopant replaces the Sb sites, the charge carriers slightly decrease due to charge compensation in the system [25].

In this study, we aim to partially incorporate indium atoms into the icosahedral voids of Co_4Sb_{12} skutterudite and partially substitute cobalt with manganese atoms. The synthesis will be conducted using the traditional melting–quenching method (MA), followed by hot pressing (HP) to create a dense pellet of the sample. We will evaluate the effect of the sintering technique on the electrical transport properties of the material.

2. Materials and Methods

The polycrystalline skutterudite $In_{0.40}Mn_{0.15}Co_{3.85}Sb_{12}$ was prepared by the ceramic method (melting method) [1]. High-purity element powders (99.99%; Aldrich, St. Louis, MO, USA) of In, Mn, Co, and Sb were mixed in an agate mortar according to the stoichiometric amounts. The reaction mixtures were sealed in evacuated quartz ampoules and placed in a tubular furnace, slowly heated at a rate of 150 °C/h and maintained at a constant temperature of 850 °C for two hours. The reaction was cooled down to room temperature, and the product was opened, ground, sealed again in evacuated quartz tubes, and annealed at 650 °C for 4 days. The final product was cooled down to room temperature. The powder sample obtained by melting and annealing was named $In_{0.40}Mn_{0.15}Co_{3.85}Sb_{12}$

(MA). To consolidate the powder-phase product ($In_{0.40}Mn_{0.15}Co_{3.85}Sb_{12}$ (MA)), it was sintered by the hot-pressing (HP) technique, using 50 MPa pressure, with a heating ramp of 10 °C/min and sintering at a temperature of 600 °C for two hours. This sample was named $In_{0.40}Mn_{0.15}Co_{3.85}Sb_{12}$ (HP). Powder pellets and hot-pressed pellets were characterized using SEM-EDX, PXRD, Raman scattering studies, and electrical properties analysis. Also, SPS-sintered Co_4Sb_{12} pellets were made to study their physical properties (600–700 °C and 50–60 MPa).

The polycrystalline phases were characterized by Powder X-ray diffraction (PXRD) at room temperature on a Bruker D8 Advance diffractometer (Bruker, Billerica, MA, USA) equipped with a CuKα radiation source in a range of $5° < 2\theta < 80°$. To determine the crystal structure of the synthesized skutterudites, XRD patterns of the samples were fitted by Rietveld refinement using Fullprof Suite software [26]. A scanning electron microscope, Bruker Vega 3 Tescan (Tescan, Brno, Czech Republic), coupled with a Quantax 400 (EDS) (Bruker, Billerica, MA, USA) microanalyzer with energy-dispersive X-ray (SEM-EDS) equipment, was employed to determine the chemical compositions and elemental distribution of the obtained skutterudites. The Raman scattering measurements were performed using a confocal Raman Witec Alpha 300 microscope (WITec GmbH, Ulm, Germany) coupled with an Ar laser of 532 nm excitation wavelength. The spectrometer was calibrated using a reference single-crystal Si sample (Raman peak at 520.7 cm^{-1}). The spectral data were collected at room temperature in the backscattering configuration in the spectral range of 100–400 cm^{-1} with a laser spot (with a power of 1.3 mW) on the sample of approximately 50×. Diffuse reflectance spectra were performed using a Jasco V-770 UV–Vis–NIR spectrophotometer (Jasco, Hachioji, Tokyo, Japan), equipped with a 60 mm integrating sphere for analyzing polycrystalline samples. The measurements were conducted over the wavelength range 200–2000 nm. The band-gap energy (Eg) was extrapolated from the linear fit of the Tauc plot [27]. The electrical properties of the (MA) sample were studied using Hall-effect measurements and ECOPIA HMS 2000 (ECOPIA, Anyang-city, Gyeonggi-do, South Korea) equipment. Powder samples were treated in a hydraulic press (at room temperature) to obtain cylindrical pellets of approximately 9 mm in diameter and 0.80–0.95 mm in thickness. The measurements were made using four gold electrical contacts. The Hall coefficient, ±0.556 T, was obtained from the linear fit of the Hall resistivity as a function of temperature (300–500 K) in an argon atmosphere.

The polycrystalline phases were characterized by Powder X-ray diffraction (PXRD) at room temperature on a Bruker D8 Advance diffractometer (Bruker, Billerica, MA, USA) equipped with a CuKα radiation source in a range of $5° < 2\theta < 80°$. To determine the crystal structure of the synthesized skutterudites, XRD patterns of the samples were fitted by Rietveld refinement using Fullprof Suite software [26]. A scanning electron microscope, Bruker Vega 3 Tescan (Tescan, Brno, Czech Republic), coupled with a Quantax 400 (EDS) (Bruker, Billerica, MA, USA) microanalyzer with energy-dispersive X-ray (SEM-EDS) equipment, was employed to determine the chemical compositions and elemental distribution of the obtained skutterudites. The Raman scattering measurements were performed using a confocal Raman Witec Alpha 300 microscope (WITec GmbH, Ulm, Germany) coupled with an Ar laser of 532 nm excitation wavelength. The spectrometer was calibrated using a reference single-crystal Si sample (Raman peak at 520.7 cm^{-1}). The spectral data were collected at room temperature in the backscattering configuration in the spectral range of 100–400 cm^{-1} with a laser spot (with a power of 1.3 mW) on the sample of approximately 50×. Diffuse reflectance spectra were performed using a Jasco V-770 UV–Vis–NIR spectrophotometer (Jasco, Hachioji, Tokyo, Japan), equipped with a 60 mm integrating sphere for analyzing polycrystalline samples. The measurements were conducted over the wavelength range 200–2000 nm. The band-gap energy (Eg) was extrapolated from the linear

fit of the Tauc plot [27]. The electrical properties of the (MA) sample were studied using Hall-effect measurements and ECOPIA HMS 2000 (ECOPIA, Anyang-city, Gyeonggi-do, South Korea) equipment. Powder samples were treated in a hydraulic press (at room temperature) to obtain cylindrical pellets of approximately 9 mm in diameter and 0.80–0.95 mm in thickness. The measurements were made using four gold electrical contacts. The Hall coefficient, ±0.556 T, was obtained from the linear fit of the Hall resistivity as a function of temperature (300–500 K) in an argon atmosphere.

3. Results and Discussion

3.1. Powder X-Ray Diffraction Analysis and SEM-EDX

The Rietveld refinement patterns and experimental data are presented in Figure 2. The experimental data were analyzed using a model in which cobalt (Co) and antimony (Sb) occupy the 8c and 24g Wyckoff positions, respectively. Indium ions partially occupy the icosahedral voids of skutterudites; these icosahedral voids were located at the 2a Wyckoff positions. The calculated Rietveld data are summarized in Table 1. The agreement parameters from the Rietveld refinement indicate that the resulting phases share the same crystalline structure as pristine $\square Co_4Sb_{12}$ (where $\square$ corresponds to the icosahedral voids at site 2a), which belongs to the *Im-3* crystalline space group. The cell parameter a of the filled skutterudites (MA and HP samples) is larger than that of the unfilled pristine c phase (see Table 1). This suggests that the presence of the manganese modifies the environment of the octahedra present in the unit cell of the material, due to the ionic radius of manganese (III) being greater than that of cobalt (III) (Mn^{III} = 79 pm; Co^{III} = 75 pm) [28]. This difference in ionic radii can lead to distortions in the crystal structure of the material. In the fitted powder X-ray diffraction (PXRD) pattern for $In_{0.40}Mn_{0.15}Co_{3.85}Sb_{12}$ (MA), shown in Figure 2a, small peaks appear below 30° (2θ), corresponding to the presence of an impurity of elemental antimony. This secondary phase of Sb accounts for 4.8% of the sample and was confirmed by Rietveld refinement of the powder pattern (Figure 2a).

Table 1. Rietveld refinement parameters obtained for $In_{0.40}Mn_{0.15}Co_{3.85}Sb_{12}$, Co_4Sb_{12}, and $In_{0.30}Sb_{0.10}Mn_{0.15}Co_{3.85}Sb_{11.90}$(HP) samples.

Phase	$\square Co_4Sb_{12}$	$In_{0.40}Mn_{0.15}Co_{3.85}Sb_{12}$ (MA)	$In_{0.40}Mn_{0.15}Co_{3.85}Sb_{12}$ (HP)	$In_{0.30}Sb_{0.10}Mn_{0.15}Co_{3.85}Sb_{11.90}$ (HP)
Space group	*Im-3*	*Im-3*	*Im-3*	*Im-3*
a (Å)	9.038 (1)	9.051 (8)	9.045 (7)	9.045 (8)
α,β,γ (°)	90	90	90	90
R-Bragg	5.7	6.7	5.2	6.0
Rf	5.4	6.2	4.2	5.1
χ^2	4.85	11.1	4.65	3.92

Figure 2b illustrates the Rietveld refinement of the hot-pressed phase $In_{0.40}Mn_{0.15}Co_{3.85}Sb_{12}$ (HP). The peaks associated with the secondary phase, which appear under 30° (2θ), are absent in the powder X-ray (PXRD) pattern of the HP phase. This indicates that the remnant elemental antimony reacted during the sintering process (HP). The PXRD technique was unable to detect other secondary phases, as the diffractometer's sensitivity was insufficient to detect small amounts of impurities. In contrast to the model, which considers the partial filling of indium into the voids, the literature reports the possibility of antimony self-insertion into the voids of undoped $\square Co_4Sb_{12}$ skutterudite. Kraemer et al. reported a self-insertion reaction induced by pressure [29]. They found that applying high pressure and high temperature during the synthesis of the $\square Co_4Sb_{12}$ phase results in a fraction of antimony being inserted into the 2a void sites [29]. In these scenarios, a second model was explored in the hot-pressed phase. In this

model, we consider partial self-insertion of antimony (Sb) and partial substitution of indium (In) at the 2a sites in the Co_4Sb_{12} phase. As a result, a filled $In_{0.30}Sb_{0.10}Mn_{0.15}Co_{3.85}Sb_{11.90}$ was the best-fitting model (Table 1, Figure S1). The results mentioned above confirm the possibility that high pressure and temperature may lead to the self-insertion of antimony into the voids of the material.

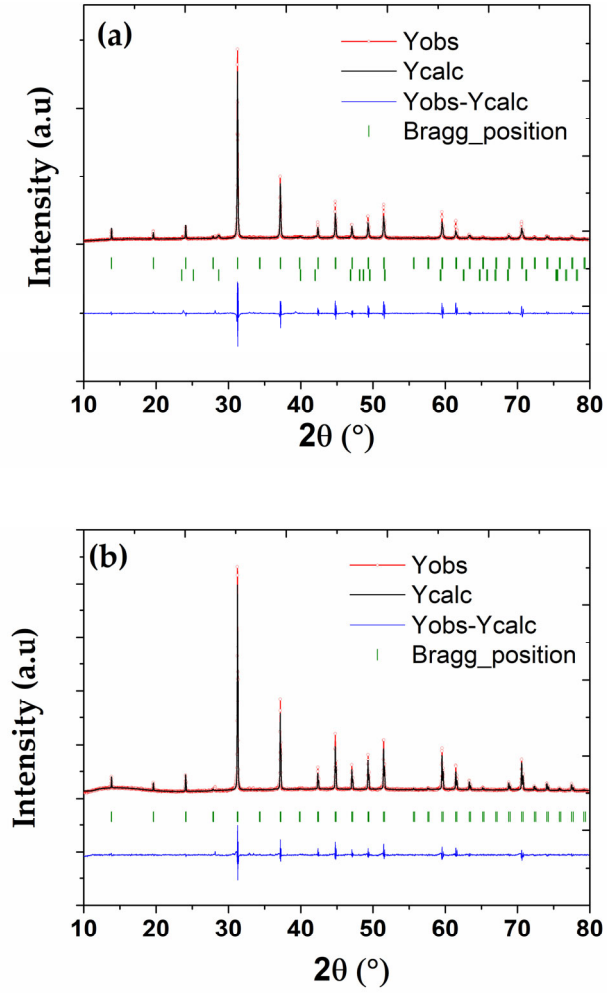


Figure 2. (**a**) Rietveld refinement of the phase $In_{0.40}Mn_{0.15}Co_{3.85}Sb_{12}$ (MA); (**b**) Rietveld refinement of the phase $In_{0.40}Mn_{0.15}Co_{3.85}Sb_{12}$ (HP) (model 1). The red dots are PXRD experimental data; the black line is the calculated fitting data; the blue line is the difference between observed and calculated data; and the green bar is the Bragg positions of the skutterudite.

Figure 3a displays the SEM mapping of $In_{0.40}Mn_{0.15}Co_{3.85}Sb_{12}$ (MA) powder sample, which illustrates the distribution of elements within the obtained phases. It shows homogeneous distribution of cobalt (Co) and antimony (Sb). However, a small quantity of unreacted indium (In) is identified in isolated regions. This observation suggests that the melting–annealing process (MA) may not be sufficient to achieve a fully homogeneous sample. The SEM mapping of the $In_{0.30}Sb_{0.10}Mn_{0.15}Co_{3.85}Sb_{11.90}$ (HP) phase reveals that hot-pressing treatment improves the homogeneity of the sample, showing a small amount of Mn and In dispersed segregations (see Figure 3b).

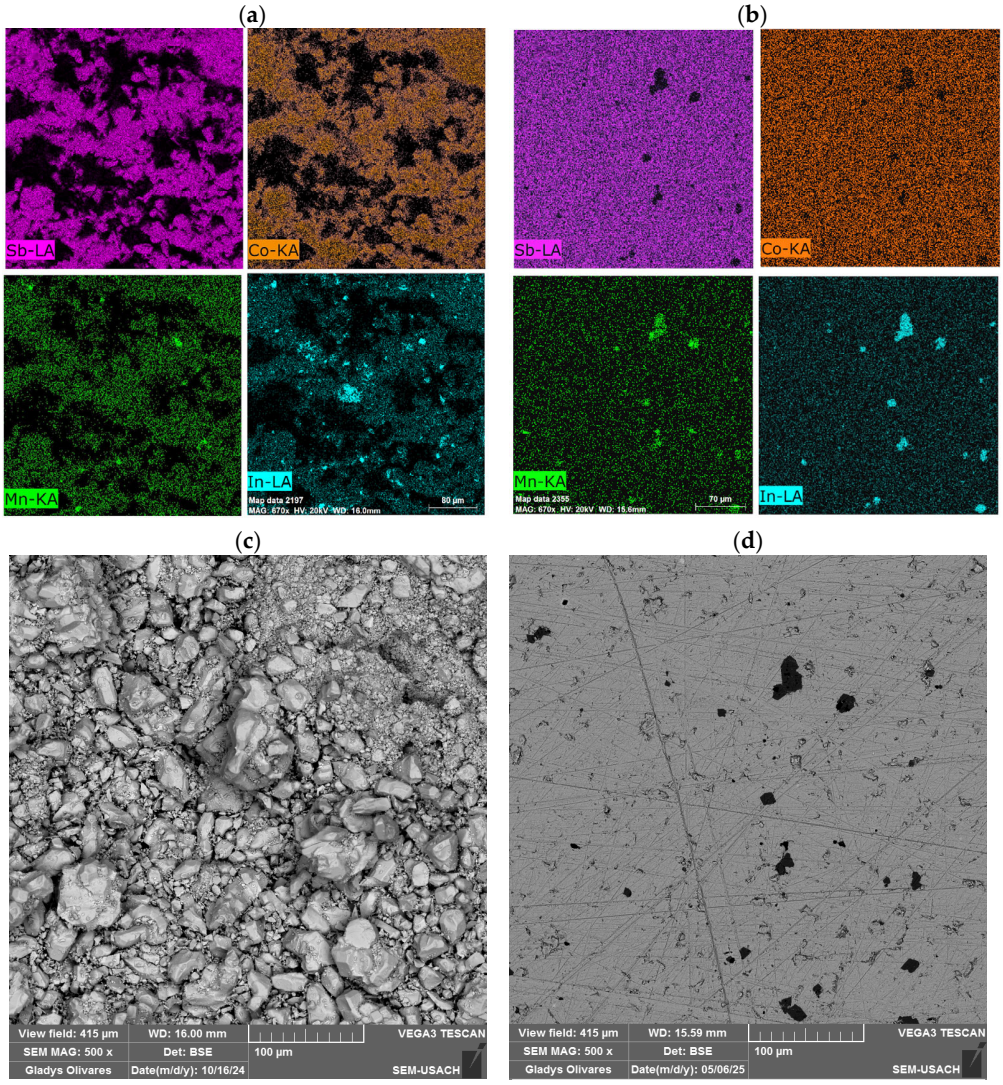


Figure 3. (**a**) SEM mapping of elements for the melted–annealed (MA) sample of $In_{0.40}Mn_{0.15}Co_{3.85}Sb_{12}$ phase; (**b**) SEM mapping of elements for the hot-pressed sample of $In_{0.40}Mn_{0.15}Co_{3.85}Sb_{12}$ phase, (**c**) BSE image of $In_{0.40}Mn_{0.15}Co_{3.85}Sb_{12}$ (MA), and (**d**) BSE image of $In_{0.30}Sb_{0.10}Mn_{0.15}Co_{3.85}Sb_{11.90}$ (HP).

3.2. Raman Spectroscopy

The irreducible representation of the optical modes for the space group corresponds to Γopt = $2A_g \oplus 2E_g \oplus 4T_g \oplus 2Au \oplus 2Eu$, where the A_g, E_g, and T_g vibrational modes are Raman-active [29–32]. The spectra of our samples were measured at room temperature with an excitation wavelength of 532 nm over the range 100–400 cm^{-1}. Figure 4a compares the Raman spectra of the polycrystalline samples $In_{0.40}Mn_{0.15}Co_{3.85}Sb_{12}$ (MA and HP) with those of the pristine phase $\square Co_4Sb_{12}$ sintered by spark plasma sintering (SPS). In the graph, it is possible to observe that the filled HP phase and the pristine SPS phase show a good correlation in the position and shape of the peaks (widths); specifically, the signals at ~110 and 125 cm^{-1} are assigned to the T_g vibrational mode, and the signal at~160 cm^{-1} is assigned to the E_g vibrational mode. On the other hand, Viennois et al. [31] reported with DFT calculations that the asymmetry of the peak observed at ~160 cm^{-1} is due to the presence of two active Raman modes, including the A_g symmetry mode. Moreover, the similarity of the broadening of the Raman peaks for the filled HP phase and the pristine SPS phase is attributed to a structural change in the pristine $\square Co_4Sb_{12}$ phase, due to the self-insertion of Sb [29,31].

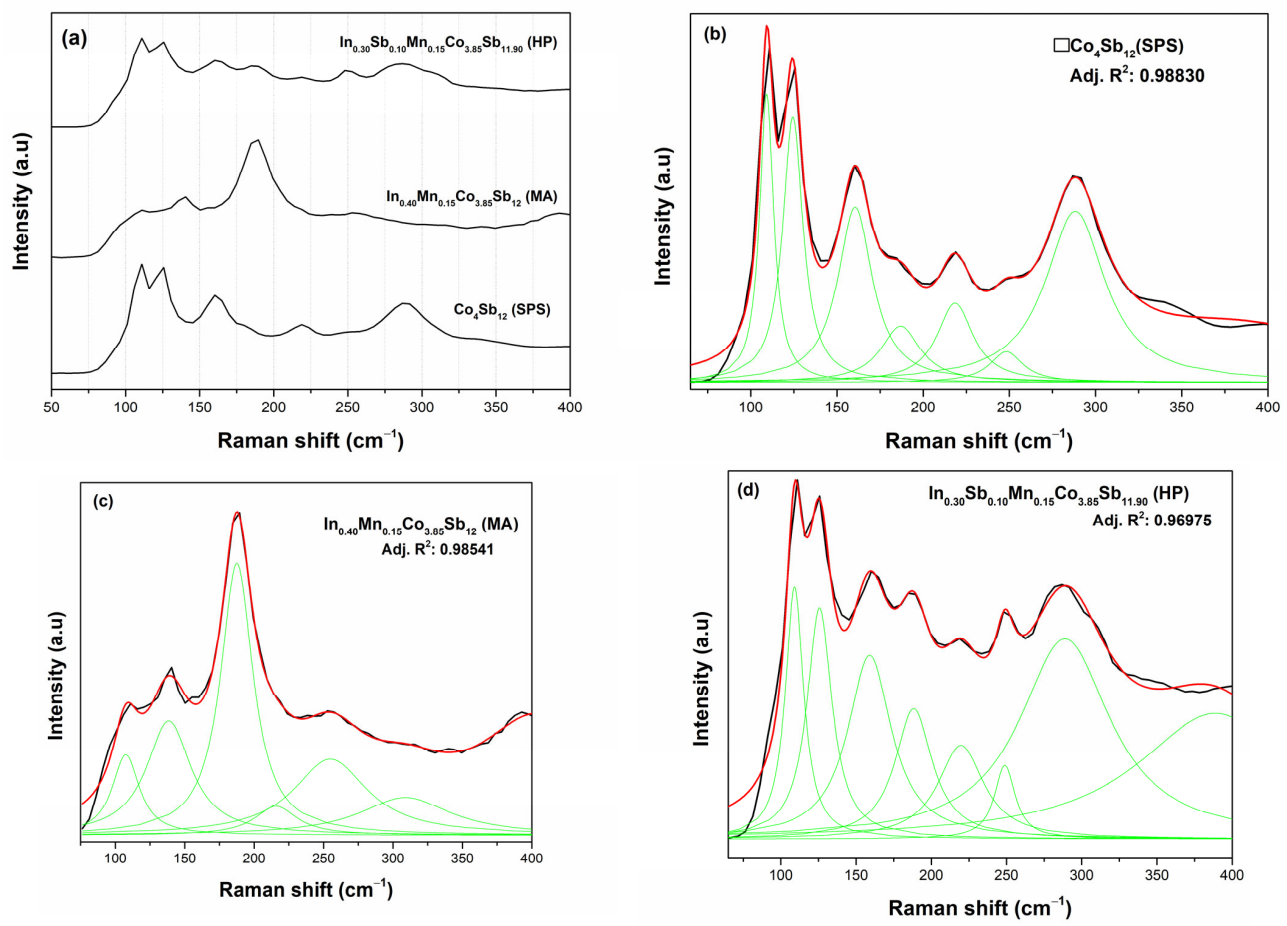


Figure 4. (**a**) Raman spectra of the Hot-pressed skutterudite samples of □Co_4Sb_{12} (SPS), $In_{0.40}Mn_{0.15}Co_{3.85}Sb_{12}$ (MA), and $In_{0.30}Sb_{0.10}Mn_{0.15}Co_{3.85}Sb_{11.90}$ (HP). (**b**) Raman spectra of □Co_4Sb_{12} (SPS), (**c**) $In_{0.40}Mn_{0.15}Co_{3.85}Sb_{12}$ (MA) and (**d**) $In_{0.30}Sb_{0.10}Mn_{0.15}Co_{3.85}Sb_{11.90}$ (HP) samples. Contribution of the different peaks deduced from the spectra. The black line represents the experimental data, while the green lines represent the contribution of the different peaks deduced from it with Lorentzian curves, and the red line shows the overall envelope fit.

For the filled phase (MA), a strong and wide main signal is observed at ~185 cm^{-1}, which we attribute to a cobalt antimonide impurity [29] or to the presence of metallic antimony, which has also been confirmed by the Rietveld refinement.

For better identification of the vibrational modes and the frequencies of these peaks, the spectra were fitted using Lorentzian curves (Figure 4b–d). In the spectra of the $In_{0.40}Mn_{0.15}Co_{3.85}Sb_{12}$ (HP) and □Co_4Sb_{12} (SPS) phases, seven signals were identified, while for the $In_{0.40}Mn_{0.15}Co_{3.85}Sb_{12}$ (MA) phase, six signals were identified. These results are summarized in Table 2, where they are compared with the results reported by Viennois et al., who used DFT calculations simulating the effect of pressurization in skutterudites, resulting in a considerable upward shift in frequencies up to ~65 cm^{-1} with respect to phases that are not subject to the effects of pressure [30].

According to the presented results, the Raman spectra allow us to infer that the sintering process via hot pressing and spark plasma sintering allows the reaction of the remaining antimony and helps the insertion of the host into the icosahedral cages. This is strengthened by the high correlation of the Raman spectra of the HP and SPS phases, where it is observed that the frequencies of the vibrational modes of the pristine phase (SPS) □Co_4Sb_{12} are identical to the frequencies of the $In_{0.30}Sb_{0.10}Mn0.15Co_{3.85}Sb_{11.90}$ phase (HP), where the Mn and Co atoms are located in the 8c site, while the In and Sb ions fill the icosahedral cages in the 2a sites. Therefore, the sintering process (applied temperature

and pressure) induces the unfilled phase sintered by SPS to experience the self-insertion of Sb, transforming it into $Sb_xCo_4Sb_{12-x}$. On the other hand, no significant changes are observed in the PXRD patterns. In line with the results obtained from the Rietveld refinement, there is an increase in the lattice parameter in $In_{0.40}Mn_{0.15}Co_{3.85}Sb_{12}$ (MA) and $In_{0.30}Sb_{0.10}Mn_{0.15}Co_{3.85}Sb_{11.90}$ (HP) in relation to the pristine phase, which can be attributed to the partial substitution of cobalt with manganese in the structure, since the radius of manganese is greater than that of cobalt [28]. On the other hand, the contribution to the increase in the lattice parameter of the chemical pressure that the guests (In and Sb) exert on the icosahedral cage from the inside must also be considered. This internal pressure promotes the expansion of the filled skutterudite structure, results that have also been reported by Kraemer et al. [29] for the $LaFe_3CoSb_{12}$ phase. Finally, we conclude that the obtained skutterudites are structurally stable.

Table 2. Frequency and proposed mode assignment of Raman peaks from skutterudites $\square Co_4Sb_{12}$, $In_{0.40}Mn_{0.15}Co_{3.85}Sb_{12}$, $In_{0.30}Sb_{0.10}Mn_{0.15}Co_{3.85}Sb_{11.90}$ and $SbCo_4Sb_{12}$.

Mode	$\square Co_4Sb_{12}$ (SPS)	$In_{0.40}Mn_{0.15}Co_{3.85}Sb_{12}$ (MA)	$In_{0.30}Sb_{0.10}Mn_{0.15}Co_{3.85}Sb_{11.90}$ (HP)	$SbCo_4Sb_{12}$ Ref. [31]
A_g	218.46	215.72	219.64	226.4
E_g	160.52	------	159.00	169.1
	248.26	254.86	248.90	231.5
T_g	109.21	107.57	109.07	77.3
	124.41	138.50	125.68	124.9
	186.88	187.54	188.26	198.3
	288.24	308.88	288.87	235.8

3.3. Optical Properties and Electrical Properties

To determine the band-gap energy of the obtained phases, diffuse reflectance spectroscopy (UV–Vis–NIR) was used. Since powder samples are strong scatterers, the absorption coefficient cannot be obtained from a transmission analysis. Instead, the diffuse reflectance R was converted into the Kubelka–Munk function: $F(R) = (1 - R)^2/2R = K/S$, where K and S are the absorption and scattering coefficients, respectively. Assuming that S is essentially constant in the absorption-edge region, F(R) is proportional to α and can be used in place of α in the Tauc relation: $(F(R)h\nu)^{1/n} = A(h\nu\text{-}Eg)$, where A is a constant, $h\nu$ is the incident photon energy, and E_g is the band-gap energy. The value of n depends on the type of band transition. $\square Co_4Sb_{12}$-based skutterudites have a direct band transition, which corresponds to $n = 1/2$ [27]. Additionally, to verify this assumption, the value of n was determined experimentally following the logarithmic analysis method proposed by Haryński et al. [27], in which a linear fit of $\ln((F(R)h\nu))$ as a function of $\ln(h\nu\text{-}Eg)$ is performed in the absorption-edge region and the exponent n is then obtained as the inverse of the slope of this fit. The values obtained for all samples are $n \approx 0.580 \pm 0.003$, confirming that these phases exhibit a direct allowed transition. The corresponding linear fits are shown in Figure S3 of the Supplementary Material. The Tauc plot of MA and hot-pressed phases is shown in Figure 5, where Eg was obtained by linear extrapolation of the absorption edge to $(F(R)h\nu))^2 = 0$. The linear fit was performed in the energy range 1.2–2.4 eV, yielding $R^2 > 0.99$ in all cases. In the literature, an experimental band-gap energy of Co_4Sb_{12} was reported with a value of Eg = 0.55 eV [32]. In this work, the phases present band gaps of $Eg = 0.750 \pm 0.006$ eV and $Eg = 0.650 \pm 0.004$ eV for $In_{0.40}Mn_{0.15}Co_{3.85}Sb_{12}$ (MA) and $In_{0.30}Sb_{0.10}Mn_{0.15}Co_{3.85}Sb_{11.90}$ (HP), respectively. These values are greater than the pristine phase Co_4Sb_{12} (0.55 eV), which indicates that chemical modification of the Co_4Sb_{12} phase modifies the band structure of the material. The larger band gaps observed in the MA

and HP phases can be attributed to the filler guest occupying the vacancies in Co_4Sb_{12}, as reported by Daehyun Wee et al. When a filler occupies a vacancy in Co_4Sb_{12}, it interacts directly with the antimony rings (Sb_4) and the antimony atoms located in the vacant space. This interaction increases the band-gap energy because the filler guest provides additional electrons to the host structure of Co_4Sb_{12} [33].

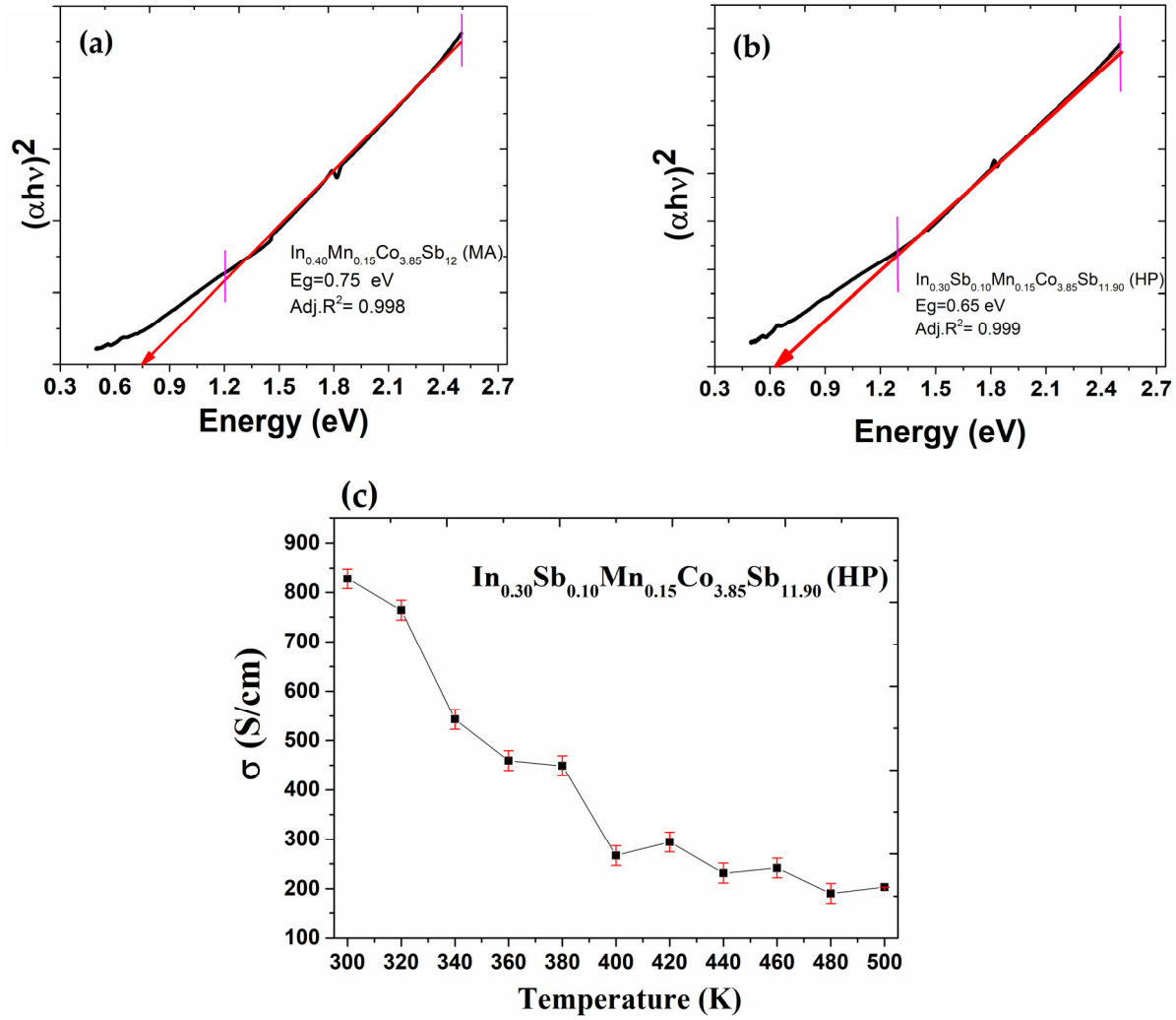


Figure 5. Tauc plots of (**a**) $In_{0.40}Mn_{0.15}Co_{3.85}Sb_{12}$ (MA) and (**b**) $In_{0.30}Sb_{0.10}Mn_{0.15}Co_{3.85}Sb_{11.90}$ (HP), and linear extrapolation of band-gap energy from each phase. (**c**) Conductivity as a function of temperature of $In_{0.30}Sb_{0.10}Mn_{0.15}Co_{3.85}Sb_{11.90}$ (HP). Red arrows are the projection of the linear fit. And pink lines indicate the linear zone range of the linear fit.

The $In_{0.40}Mn_{0.15}Co_{3.85}Sb_{12}$ (MA and HP) samples showed *n*-type conductivity at room temperature (RT). The Hall coefficients were negative, with a carrier concentration of approximately ~10^{19} cm^{-3}. The carrier concentration values of $In_{0.40}Mn_{0.15}Co_{3.85}Sb_{12}$-MA ($3.10 \times 10^{19}$ cm^{-3}) and $In_{0.30}Sb_{0.10}Mn_{0.15}Co_{3.85}Sb_{11.90}$ (1.98×10^{19} cm^{-3}) are 10 times higher than those reported in the unfilled □Co_4Sb_{12} pristine phase (1.16×10^{18} cm^{-3}) [34]. Park K.-H. et al. reported values of approximately 3.50×10^{20} cm^{-3} for Co_4Sb_{12} single-doped with manganese ($Mn_{0.5}Co_{3.5}Sb_{12}$), which showed typical *p*-type semiconductor behavior [25]. Therefore, indium doping is mainly responsible for the n-type conduction in the $In_{0.40}Mn_{0.15}Co_{3.85}Sb_{12}$ system. In addition, He T. et al. have reported that skutterudites single-filled with indium ($In_yCo_4Sb_{12}$), using different concentrations of indium (y = 0.0–3.0), show *n*-type behavior [35]. This behavior indicates that indium

is an electron donor in chemical substitution on the skutterudite *p*-type Co_4Sb_{12} phase. Electrical mobility is an important property for evaluating electrical behavior. The electrical mobilities of $In_{0.40}Mn_{0.15}Co_{3.85}Sb_{12}$ MA and $In_{0.30}Sb_{0.10}Mn_{0.15}Co_{3.85}Sb_{11.90}$ HP samples (MA~10^{-1} $cm^2/V{\cdot}s$; HP~10^1 $cm^2/V{\cdot}s$) were smaller than the experimental value for Co_4Sb_{12} (2835 $cm^2/V{\cdot}s$). The In/Mn chemical substitution thus led to low mobility. The electrical conductivity of $In_{0.40}Mn_{0.15}Co_{3.85}Sb_{12}$-MA (1.35 S/cm) was lower than the value obtained for pristine Co_4Sb_{12} (528 S/cm) at RT. These values suggest that σ is sensitive to the contents of In and Mn. However, the hot-pressed $In_{0.30}Sb_{0.10}Mn_{0.15}Co_{3.85}Sb_{11.90}$ sample shows a significant increase (~10^2 times) in electrical conductivity in comparison with the MA phase, indicating a grain boundary effect due to the increase in particle size during the sintering process [36]. Furthermore, the hot-pressing process promotes the homogenization of the "self-inserted" Sb, thereby optimizing the conduction path. The electrical conductivity of the MA phase exhibits an increase with the rise in temperature, demonstrating characteristics typical of intrinsic semiconductors. In contrast, the hot-pressed $In_{0.30}Sb_{0.10}Mn_{0.15}Co_{3.85}Sb_{11.90}$ **(**HP) sample displays a significant reduction in electrical conductivity as temperature increases. This behavior is generally associated with degenerate semiconductor materials (see Figure 5c).

4. Conclusions

$In_{0.40}Mn_{0.15}Co_{3.85}Sb_{12}$ skutterudite phase was obtained by the ceramic method (melting and annealing, MA) and the hot-pressing method (HP). Rietveld refinement confirms the partially substitution of the cobalt sites with manganese in the skutterudite structure. Additionally, according to the Rietveld refinement of the hot-pressed sample, two structural models are proposed: (i) the partial indium insertion and partial substitution of cobalt with manganese to obtain the $In_{0.40}Mn_{0.15}Co_{3.85}Sb_{12}$ phase and (ii) the pressure-induced self-insertion of antimony into the voids (2a sites), resulting in the best fit for the $In_{0.30}Sb_{0.10}Mn_{0.15}Co_{3.85}Sb_{11.90}$ phase. SEM-EDS mapping suggests that the hot-pressing technique favored the formation of homogeneous samples. The vibrational Raman analyses of $In_{0.40}Mn_{0.15}Co_{3.85}Sb_{12}$ (MA) and $In_{0.30}Sb_{0.10}Mn_{0.15}Co_{3.85}Sb_{11.90}$ (HP) are in good agreement with the skutterudite crystal structure and correlate well with the pristine $\square Co_4Sb_{12}$ phase. A vibrational mode at 185 cm^{-1} in $In_{0.40}Mn_{0.15}Co_{3.85}Sb_{12}$ (MA) is associated with antimony impurities, which is confirmed by Rietveld refinement. Raman spectra of the HP sample are well correlated with the (SPS) $\square Co_4Sb_{12}$ phase, indicating structural changes due to self-insertion of antimony into the voids. Electrical measurements indicate n-type semiconductor behavior (MA and HP methods) and band-gap values ranging from 0.750 eV to 0.650 eV. The band-gap energy of both MA and HP samples is greater than that of the unfilled Co_4Sb_{12} pristine phase. Charge carriers of both obtained phases (MA and HP) are one order of magnitude (~10^{19} cm^{-3}) greater than the pristine Co_4Sb_{12} phase (~10^{18} cm^{-3}), suggesting that the addition of indium as a filler acts as an electron donor. The hot-pressed $In_{0.30}Sb_{0.10}Mn_{0.15}Co_{3.85}Sb_{11.90}$ sample shows a significant increase (~10^2 times) in conductivity, making the material much more conductive and exhibiting metallic/degenerate behavior in the sintered (HP) phase. This is attributed to a grain boundary effect resulting from the increase in particle size, which optimizes the conduction path.

Supplementary Materials: The following supporting information can be downloaded at: https://www.mdpi.com/article/10.3390/app16115259/s1. Figure S1: Rietveld refinement of $In_{0.30}Sb_{0.10}Mn_{0.15}Co_{3.85}Sb_{11.9}$ phase (HP). Figure S2: EDX and mass percent of elements of $In_{0.40}Mn_{0.15}Co_{3.85}Sb_{12}$ (MA). Figure S3: Linear fit of Log(αhν) as a function of hν plots.

Author Contributions: Conceptualization, P.V.-G. and C.C.; methodology and experiments, C.C., N.A. and P.V.-G.; writing—original draft preparation, S.M., P.V.-G. and C.C.; electrical measurements, C.C.; optical properties, R.C. All authors have read and agreed to the published version of the manuscript.

Funding: This research study is supported by Agencia Nacional de Investigación y Desarrollo, grant number: Anid-Fondecyt Postdoctorado 3220312.

Institutional Review Board Statement: Not applicable.

Informed Consent Statement: Not applicable.

Data Availability Statement: The data presented in this study are available in the article.

Acknowledgments: The authors acknowledge the financial support from FONDECYT-ANID Postdoctoral project 3220312 (Catalina Cortés) and FONDEQUIP grant EQM140142 for Raman Witec Alpha 300 equipment. We would like to thank Antonio Gadámez for his contributions and the fruitful discussion of the experimental results.

Conflicts of Interest: The authors declare no conflicts of interest.

References

1. Bell, L.E. Cooling, Heating, Generating Power, and Recovering Waste Heat with Thermoelectric Systems. *Science* **2008**, *321*, 1457–1461. [CrossRef] [PubMed]
2. Xu, N.; Xu, Y.; Zhu, J. Topological Insulators for Thermoelectrics. *npj Quantum Mater.* **2017**, *2*, 51. [CrossRef]
3. Hu, G.; Madusanka, P.; Dhawan, R.; Xie, W.; Debord, J.; Tran, T.; Maggio, K.; Edwards, H.; Lee, M. Scaling of Power Generation with Dopant Density in Integrated Circuit Silicon Thermoelectric Generators. *IEEE Electron Device Lett.* **2019**, *40*, 1917–1920. [CrossRef]
4. d'Angelo, M.; Galassi, C.; Lecis, N. Thermoelectric Materials and Applications: A Review. *Energies* **2023**, *16*, 6409. [CrossRef]
5. Goldsmid, H.J. The Thermoelectric and Related Effects. In *Introduction to Thermoelectricity*; Springer Series in Materials Science; Springer: Berlin/Heidelberg, Germany, 2016; Volume 121, pp. 1–7. [CrossRef]
6. Sootsman, J.R.; Chung, D.Y.; Kanatzidis, M.G. New and Old Concepts in Thermoelectric Materials. *Angew. Chem.—Int. Ed.* **2009**, *48*, 8616–8639. [CrossRef]
7. Vining, C.B. An Inconvenient Truth about Thermoelectrics. *Nat. Mater.* **2009**, *8*, 83–85. [CrossRef]
8. Snyder, G.J.; Toberer, E.S. Complex Thermoelectric Materials. *Nat. Mater.* **2008**, *7*, 105–114. [CrossRef]
9. Yox, P.; Viswanathan, G.; Sarkar, A.; Wang, J.; Kovnir, K. Thermoelectric Materials. In *Comprehensive Inorganic Chemistry III*, 3rd ed.; Elsevier: Amsterdam, The Netherlands, 2023; Volume 1–10, pp. 45–79, ISBN 9780128231531.
10. Rogl, G.; Rogl, P. Skutterudites, a most promising group of thermoelectric materials. *Curr. Opin. Green Sustain. Chem.* **2017**, *4*, 50–57. [CrossRef]
11. Zhou, X.Y.; Yan, Y.C.; Lu, X.; Zhu, H. Routes for high-performance thermoelectric materials. *Mater. Today* **2018**, *21*, 974–988. [CrossRef]
12. Oftedal, I. XXXIII. Die Kristallstruktur von Skutterudit und Speiskobalt-Chloanthit. *Z. Für Krist.-Cryst. Mater.* **1928**, *66*, 517–546. [CrossRef]
13. Nolas, G.S.; Morelli, D.T.; Tritt, T.M. SKUTTERUDITES: A Phonon-Glass-Electron Crystal Approach to Advanced Thermoelectric Energy Conversion Applications. *Annu. Rev. Mater. Sci.* **1999**, *29*, 89–116. [CrossRef]
14. Zhang, J.J.; Xu, B.; Wang, L.M.; Yu, D.; Liu, Z.; He, J.; Tian, Y. Great thermoelectric power factor enhancement of $CoSb_3$ through the lightest metal element filling. *Appl. Phys. Lett.* **2011**, *98*, 072109. [CrossRef]
15. Chen, L.D.; Kawahara, T.; Tang, X.F.; Goto, T.; Hirai, T.; Dyck, J.S.; Chen, W.; Uher, C. Anomalous barium filling fraction and n-type thermoelectric performance of BayCo4Sb12. *J. Appl. Phys.* **2001**, *90*, 1864–1868. [CrossRef]
16. Li, Y.L.; Qiu, P.F.; Duan, H.Z.; Chen, J.; Snyder, G.J.; Shi, X.; Iversen, B.B.; Chen, L. Enhanced thermoelectric performance in rare-earth filled-skutterudites. *J. Mater. Chem. C.* **2016**, *4*, 4374–4379. [CrossRef]
17. Pei, Y.Z.; Yang, J.; Chen, L.D.; Zhang, W.; Salvador, J.R.; Yang, J. Improving thermoelectric performance of caged compounds through light-element filling. *Appl. Phys. Lett.* **2009**, *95*, 042101. [CrossRef]
18. Chernyshova, E.; Voronin, A.; Moskovskikh, D.; Sviridova, T.; Yushchuk, V.; Khovaylo, V. Thermoelectric Properties of Filled $InCo_4Sb_{12}$ Skutterudite with Embedded ZnO Inclusions: Influence on Thermal Conductivity and Stability of Electrical Properties. *Ceram. Int.* **2024**, *50*, 55201–55207. [CrossRef]
19. Mallik, R.C.; Jung, J.Y.; Ur, S.C.; Kim, I.H. Thermoelectric Properties of $In_zCo_4Sb_{12}$ Skutterudites. *Met. Mater. Int.* **2008**, *14*, 223–228. [CrossRef]

20. Mallik, R.C.; Stiewe, C.; Karpinski, G.; Hassdorf, R.; Müller, E. Thermoelectric Properties of Co_4Sb_{12} Skutterudite Materials with Partial in Filling and Excess in Additions. *J. Electron. Mater.* **2009**, *38*, 1337–1343. [CrossRef]
21. Khovaylo, V.V.; Korolkov, T.A.; Voronin, A.I.; Gorshenkov, M.V.; Burkov, A.T. Rapid Preparation of $In_xCo_4Sb_{12}$ with a Record-Breaking ZT = 1.5: The Role of the In Overfilling Fraction Limit and Sb Overstoichiometry. *J. Mater. Chem. A Mater.* **2017**, *5*, 3541–3546. [CrossRef]
22. Kim, I.H.; Ur, S.C. Electronic Transport Properties of Fe-Doped $CoSb_3$ Prepared by Encapsulated Induction Melting. *Mater. Lett.* **2007**, *61*, 2446–2450. [CrossRef]
23. Bertini, L.; Stiewe, C.; Toprak, M.; Williams, S.; Platzek, D.; Mrotzek, A.; Zhang, Y.; Gatti, C.; Müller, E.; Muhammed, M.; et al. Nanostructured $Co_{1-X}Ni_xSb_3$ Skutterudites: Synthesis, Thermoelectric Properties, and Theoretical Modeling. *J. Appl. Phys.* **2003**, *93*, 438–447. [CrossRef]
24. Bourgès, C.; Zhang, W.; Raut, K.K.; Owada, Y.; Kawamoto, N.; Mitome, M.; Kobayashi, K.; Halet, J.F.; Berthebaud, D.; Mori, T. Investigation of Mn Single and Co-Doping in Thermoelectric $CoSb_3$-Skutterudite: A Way Toward a Beneficial Composite Effect. *ACS Appl. Energy Mater.* **2023**, *6*, 9646–9656. [CrossRef]
25. Park, K.-H.; Kim, I.-H. Thermoelectric Properties of $Co_{4-X}Mn_xSb_{12-Y}Sn_y$ Skutterudites. *Electron. Mater. Lett.* **2011**, *7*, 39–43. [CrossRef]
26. Rodríquez-Carvajal, J.; Roisnel, T. Line Broadening Analysis Using FullProf*: Determination of Microstructural Properties. *Mater. Sci. Forum* **2004**, *443–444*, 123–126. [CrossRef]
27. Haryński, Ł.; Olejnik, A.; Grochowska, K.; Siuzdak, K. A facile method for Tauc exponent and corresponding electronic transitions determination in semiconductors directly from UV–Vis spectroscopy data. *Opt. Mater.* **2022**, *127*, 112205. [CrossRef]
28. Miessler, G.L.; Donald, A.T. Inorganic Chemistry, Appendix B-1: Ionic Radii. In *Inorganic Chemistry*; Pearson Education International: London, UK, 2004; p. 668, ISBN 0136153836.
29. Kraemer, A.C.; Gallas, M.R.; Da Jornada, J.A.H.; Perottoni, C.A. Pressure-Induced Self-Insertion Reaction in $CoSb_3$. *Phys. Rev. B* **2007**, *75*, 024105. [CrossRef]
30. Nolas, G.S.; Kendziora, C.A. Raman Spectroscopy Investigation of Lanthanide-Filled and Unfilled Skutterudites. *Phys. Rev. B* **1999**, *59*, 6189–6192. [CrossRef]
31. Viennois, R.; Kume, T.; Komura, M.; Girard, L.; Haidoux, A.; Rouquette, J.; Koza, M.M. Raman-Scattering Experiments on Unfilled Skutterudite $CoSb_3$ under High Pressure and High Temperature. *J. Phy. Chem. C* **2020**, *124*, 23004–23012. [CrossRef]
32. Nolas, G.S.; Slack, G.A.; Caillat, T.; Meisner, G.P. Raman Scattering Study of Antimony-Based Skutterudites. *J. Appl. Phys.* **1996**, *79*, 2622–2626. [CrossRef]
33. Wee, D.; Kozinsky, B.; Marzari, N.; Fornari, M. Effects of Filling in $CoSb_3$: Local Structure, Band Gap, and Phonons from First Principles. *Phys. Rev. B Condens. Matter Mater. Phys.* **2010**, *81*, 045204. [CrossRef]
34. Caillat, T.; Borshchevsky, A.; Fleurial, J.P. Properties of Single Crystalline Semiconducting $CoSb_3$. *J. Appl. Phys.* **1996**, *80*, 4442–4449. [CrossRef]
35. He, T.; Chen, J.; Rosenfeld, H.D.; Subramanian, M.A. Thermoelectric Properties of Indium-Filled Skutterudites. *Chem. Mater.* **2006**, *18*, 759–762. [CrossRef]
36. Nakagawa, H.; Tanaka, H.; Kasama, A.; Anno, H.; Matsubara, K. Grain Size Effects on Thermoelectric Properties of Hot-Pressed $CoSb_3$. In *16th International Conference on Thermoelectrics (Cat. No.97TH8291)*; IEEE: Dresden, Germany, 1997; pp. 351–355, ISBN 0-7803-4057-4.

Disclaimer/Publisher's Note: The statements, opinions and data contained in all publications are solely those of the individual author(s) and contributor(s) and not of MDPI and/or the editor(s). MDPI and/or the editor(s) disclaim responsibility for any injury to people or property resulting from any ideas, methods, instructions or products referred to in the content.